

# Enhanced properties of graphene/fly ash geopolymeric composite cement

Mohamed Saafi<sup>1\*</sup>, Leung Tang<sup>2</sup>, Jason Wang<sup>1</sup>, Mahbubur Rahman<sup>1</sup> and John Liggat<sup>3</sup>

<sup>1</sup>Department of Civil and Environmental Engineering, University of Strathclyde, G4 0NG, UK

<sup>2</sup>Agilent Technologies, -EH12 9DJ, UK

<sup>3</sup>Department of Pure and Applied Chemistry, University of Strathclyde, G4 0NG, UK

## Abstract

This paper reports for the first time the incorporation of in-situ reduced graphene oxide (rGO) into geopolymers. The resulting rGO-geopolymeric composites are easy to manufacture and exhibit excellent mechanical properties. Geopolymers with graphene oxide (GO) contents of 0.00, 0.10, 0.35 and 0.50% by weight were fabricated. The functional groups, morphology, void filling mechanisms and mechanical properties of the composites were determined. The Fourier transform infrared (FTIR) spectra revealed that the alkaline solution reduced the hydroxyl/carbonyl groups of GO by deoxygenation and/or dehydration. Concomitantly, the spectral absorbance related to silica type cross-linking increased in the spectra. The scanning electron microscope (SEM) micrographs indicated that rGO altered the morphology of geopolymers from a porous nature to a substantially pore filled morphology with increased mechanical properties. The flexural tests showed that 0.35-wt% rGO produced the highest flexural strength, Young's modulus and flexural toughness and they were increased by 134%, 376% and 56%, respectively.

Keywords: C. Mechanical Properties, D. Alkali Activated Cement, E. Composite, D, Reinforcement.

\* Corresponding author: [m.bensalem.saafi@strath.ac.uk](mailto:m.bensalem.saafi@strath.ac.uk), Tel: 44 (0) 141 548 4569

## 1. Introduction

In recent years, considerable research has been aimed at the development of fly ash based geopolymers. This is driven by the need to reduce or complement the ordinary Portland

30 cement (OPC) consumption in the construction industry. OPC is major contributor to green-  
31 house gases when compared to geopolymers. Geopolymers in general emit less green-house  
32 gases due to their lower calcium carbonate-based raw materials and production temperature.  
33 Geopolymers are inorganic polymers synthesized via a chemical reaction between a highly  
34 alkaline solution and the Si-Al minerals present in the fly ash. This results in a 3-D polymeric  
35 network consisting of Si-O-Al-O bonds with the formula of  $M_n[-(SiO_2)_z - AlO_2]_w H_2O$   
36 where  $M$  is an alkaline element,  $n$  is the degree of polymerization,  $z$  is a value between 1 and  
37 32, and  $w$  is the hydration extent, which is a function of the type and amount of the alkaline  
38 solution used [1]. The most commonly used alkaline solution is a mixture of sodium silicate  
39 ( $Na_2SiO_3$ ) and sodium hydroxide (NaOH) with a  $Na_2SiO_3/NaOH$  ratio between 1.5 and 3 [2].  
40 The processed type F fly ash based geopolymers exhibit mechanical properties similar to  
41 those of OPC but with better performance under severe environmental conditions. For  
42 example, it has been reported that geopolymers exhibit excellent resistance to acid and sulfate  
43 attack when compared to OPC due to the lower calcium content of the fly ash [3-5]. Fly ash  
44 based geopolymers are also fire resistant binders. According to Pan et al. [6], geopolymers  
45 are inherently fire resistant due their polymeric-silicon-oxygen-aluminum framework. Pan et  
46 al. [6] and Duxson et al. [7] have shown that geopolymers can sustain high temperatures (up  
47 to 800°C) with little gel structural degradation.  
48 OPC and geopolymers are typically brittle and characterized by low tensile strength and  
49 fracture toughness. To combat this, OPC and geopolymers are often reinforced with micro  
50 and nano fibers. For example, fibers such as steel, polypropylene (PP), polyvinyl chloride  
51 (PVC) and basalt fibers have been found to be particularly effective in controlling crack  
52 propagation and enhancing the flexural strength and the fracture energy of geopolymers [8].  
53 These enhanced properties were mainly attributed to the fiber bridging effect during both  
54 micro and macro cracking of the geopolymeric matrix [8]. The mechanical interlocking at the

55 fiber-matrix interface and chemical bonding between the fiber and the matrix both play a role  
56 in strengthening and toughening of the geopolymeric matrix [9].

57 Recently, carbon nanotubes (CNTs) were adopted as a reinforcement for geopolymers.  
58 The unique properties such as high elastic modulus and tensile strength and high aspect ratio  
59 make CNTs an ideal candidate for reinforcement. Mackenzie and Bolton [10] investigated  
60 the tensile strength of potassium-based aluminosilicate (clay) geopolymers containing single  
61 walled carbon nanotubes (SWCNTs) at concentrations of 0.20, 0.25 and 0.35-wt%. The  
62 tensile strength results were inconsistent. The tensile strength decreased, and then increased  
63 before it began to decrease again. Saafi et al. [11] studied the multifunctional properties of  
64 geopolymers containing multiwalled carbon nanotubes (MWCNTs). Their experimental  
65 results indicated that the incorporation of MWCNTs up to 0.5-wt% enhanced the flexural  
66 strength, the Young's modulus, the flexural toughness and the fracture energy of  
67 geopolymers. This improvement was due to a variety of CNT strengthening and toughening  
68 mechanisms, including high resistance to crack coalescence, crack deflection at the  
69 CNT/matrix interface, inducing and bridging of multiple cracks and CNT pullout on the  
70 fractured surfaces [12].

71 A non-aggregated dispersion of CNTs in aqueous liquid media is a prerequisite for their  
72 use as reinforcing fillers in cement and geopolymer based composites. However, dispersion  
73 of CNTs in water is highly challenging as van der Waals forces between the CNTs create  
74 bundles and agglomerates. For CNTs, this phenomenon reduces the workability and  
75 mechanical properties of composites [13, 14]. Graphene offers many benefits over CNTs,  
76 including higher surface area (due to its 2-dimensional structure) and strong mechanical  
77 interaction with the hosting matrix resulting from the wrinkling [15]. However, graphene  
78 sheets exhibit very low dispersibility in polar liquids due to their high surface area and surface

79 energy and, as a result, they agglomerate and stick to each other, thereby reducing their  
80 reinforcement effects when agglomerated [16].

81 Graphene oxide (GO), the oxidized form of graphite has been considered as a precursor for  
82 bulk-scale production of low-cost graphene-based materials [17]. GO sheets contain a large  
83 concentration of hydroxyl, epoxide, carboxyl and carbonyl functional groups [18]. These  
84 functional groups are compatible with water and therefore the GO is highly dispersible in  
85 polar liquids [19]. GO-based fillers were incorporated into various plastic and organic  
86 composites [20, 21]. The improved mechanical properties of these composites were attributed  
87 to the high specific surface area and excellent mechanical properties of GO sheets [21].

88 In view of these outstanding properties, the integration of graphene into geopolymers can  
89 significantly improve their properties and provide them with self-sensing capabilities. The  
90 objective of this paper is to investigate the mechanical properties, chemical functional group  
91 changes and morphological changes of geopolymers containing reduced GO (rGO) sheets at a  
92 variety of loadings. The properties discussed herein are the morphology characteristics, the  
93 flexural strength, the Young's modulus, the flexural toughness and the void and pore filling  
94 mechanisms together with chemical changes associated with the alkaline reduction of GO.

## 95 **2. Experimental program**

### 96 *2.1. Materials*

97 Class F fly ash was used to process the rGO-geopolymeric composites. The chemical  
98 composition of the fly ash is given in Table 1. Based on the size distribution tests conducted  
99 by the supplier, 70% by weight of the total type F fly ash spherical particles were between 0.2  
100 and 5 $\mu$ m in diameter.

101 Hydrophilic and oxygenated 1.1 nm thick pristine GO sheets (0.5 – 5 $\mu$ m with purity higher  
102 than 90%, supplied by Supermarket®) were employed in this study. The required GO content  
103 was dispersed in deionized water by using a 100W Cell Disruptor for 1.5 hours. The plain

104 geopolymeric matrix had a bulk of density of  $2.0 \text{ g/cm}^3$  and composed of 72-wt% fly ash, 20-  
105 wt% of sodium silicate ( $\text{Na}_2\text{SiO}_3$  with 29.4%  $\text{SiO}_2$ , 14.7%  $\text{NaO}_2$  and 59.9%  $\text{H}_2\text{O}$ ) and 8-wt%  
106 of 10M sodium hydroxide ( $\text{NaOH}$ ). The ( $\text{Na}_2\text{SiO}_3 + \text{NaOH}$ ) to fly ash ratio was 0.39.

## 107 *2.2. Fabrication of rGO-geopolymeric composites*

108 To chemically reduce the GO sheets during mixing and curing, the dispersed pristine GO  
109 sheets were first added to 100g of  $\text{NaOH}$  solution (10M) and mildly sonicated for 1 hour.  
110 The stable and heterogeneous mixture was then mixed with the fly ash and the left over  
111 chemicals ( $\text{Na}_2\text{SiO}_3 + \text{NaOH}$ ) for 1 minute. Subsequently, the mix was subjected to  
112 sonication for 3 minutes prior to casting the beams. Geopolymeric beams (50 mm x 50 mm x  
113 350 mm) containing different concentrations of rGO (0.00, 0.10, 0.35 and 0.50-wt%) were  
114 prepared. The molded geopolymeric beams were first cured at a room temperature of  $25^\circ\text{C}$  for  
115 2 hours and then placed in an oven for 24 hours at constant temperature of  $60^\circ\text{C}$ .

## 116 *2.3. Morphology and chemical characterization*

117 The morphology of the rGO-geopolymeric composites and the rGO sheets were examined  
118 with a scanning electron microscope (SEM). SEM observations were also performed on the  
119 rGO-geopolymeric suspensions in order to identify their morphology during processing. An  
120 Agilent Technologies Exoscan 4100 Fourier transform mid-infrared spectrometer, with  
121 diffuse sample interface, was used to collect infrared diffuse spectra. The instrumental  
122 conditions for spectral collection were 128 scans at a resolution of  $8 \text{ cm}^{-1}$ . The spectral  
123 changes both in terms of size and position were used to identify the processes and chemical  
124 changes in the pristine GO sheets and geopolymeric composites. In addition, the  
125 geopolymeric gels and the rGO sheets were also studied with particular attention paid to the  
126 chemical bonding and functional groups present.

127

128

## 129 2.4. Mechanical characterization

130 In total, 10 geopolymeric beams per rGO content were prepared for the mechanical  
131 characterization. The beams had a clear span of 210 mm and a distance between the two  
132 loading contacts of 70 mm. The beams were subjected to four-point bending tests to  
133 determine the mechanical properties; namely, flexural strength, Young's modulus and flexural  
134 toughness. The four-point bending tests were conducted under displacement control with a  
135 rate of 0.05 mm/min. During testing, load and deflection at the center were recorded  
136 continuously. The flexural strength ( $\sigma_f$ ) and the Young's modulus ( $E$ ) were calculated as:

$$137 \quad \sigma_f = \frac{3Pa}{b^3} \quad (1)$$

$$138 \quad E = m \frac{a(3l^2 - 4a^2)}{4b^4} \quad (2)$$

139 where  $P$  is the maximum applied load,  $l$  is the length of the beam between the supports,  $a$  is  
140 the distance between the support and the loading point,  $b$  is the width and thickness of the  
141 beam and  $m$  is the slope of the tangent to the straight-line portion of the load-deflection curve.

142 The flexural toughness of the beams is the total area under the stress-strain curve obtained  
143 from Eqs. 1 and 3, where Eq. 3 is given by:

$$144 \quad \varepsilon = \frac{12b\Delta}{3b^2 - 4a^2} \quad (3)$$

145 where  $\varepsilon$  is the tensile strain and  $\Delta$  is the displacement recorded by the LVDT.

## 146 3. Results and discussion

### 147 3.1. FTIR analysis and chemical characterization

148 Figure 1 depicts the FTIR spectrum of the fly ash, (black dashed line), pristine GO sheets  
149 (yellow solid line), plain geopolymers (red dash-dotted line) and rGO-geopolymers with 0.35-  
150 wt% (blue dotted line). The FTIR spectrum of the fly ash is dominated by two overlapping  
151 peaks corresponding to Si-O (doublet) and Al-O functional groups or bonds in the range of

152 800 to 1200  $\text{cm}^{-1}$ . These groups are clearly observed in the spectra as shown in Fig. 2. The  
153 Si-O and Al-O overlapping (negative) reststrahlen peaks represent the main mineral content of  
154 the fly ash (see Table 1) and are much greater than the C-H stretching modes that are the two  
155 downward peaks in the spectral region of 3000-2850  $\text{cm}^{-1}$ . The organic content (C-H) of the  
156 fly ash is much smaller than the mineral content (Si-O and Al-O) in good agreement with  
157 Table 1. The reststrahlen peak absorbances at  $\sim 1800\text{-}1700 \text{ cm}^{-1}$  are the result of the presence of  
158 other organic functional groups in the fly ash, namely carbonyl type species. Finally, a  
159 variety of hydrogen bonded -OH functional groups derived from Al-OH, Si-OH and C-OH  
160 exist in the dried fly ash as evidenced by the complexity of the peak shape in -OH functional  
161 group (3000-3700  $\text{cm}^{-1}$ ).

162 From Fig. 1, it can be seen that the pristine GO sheets contain high concentrations of  
163 hydroxyl (at 3000-3700  $\text{cm}^{-1}$  and  $\sim 1600 \text{ cm}^{-1}$ ) and carbonyl ( $\sim 1700 \text{ cm}^{-1}$ ) functional groups.  
164 The FTIR spectrum of the unreduced GO sheets also displays the existence of  
165 methyl/methylene ( $\text{CH}_2/\text{CH}_3$ ) stretches between 3000 and 2800  $\text{cm}^{-1}$ . These groups are  
166 concentrated at the edges of the GO sheets.

167 For both geopolymers (red line or blue line in Fig. 1 – with or without GO), the alkaline  
168 activator ( $\text{NaOH} + \text{Na}_2\text{SiO}_3$ ) changed the fly ash hydroxyl spectral absorbance peak shape  
169 from a complex distribution to a near homogeneous hydroxyl functional group. These  
170 chemical changes are due to the loss of the peak as a consequence of bond destruction. Figure  
171 1 indicates a distinct shape change for the -OH from the base fly ash to the geopolymer. It  
172 also shows that the alkaline activator changed the distribution of the Al-O/Si-O regions at  
173 800-1200  $\text{cm}^{-1}$  for both geopolymers. The addition of sodium silicate increased the relative  
174 concentration of Si-O in the geopolymeric matrix. As expected due to the presence of rGO,  
175 the rGO geopolymers exhibited higher organic contents at  $\sim 1500 \text{ cm}^{-1}$  as compared to the  
176 plain geopolymers. These negative/derivative peak shapes are caused by concomitant

177 changes in the refractive index with the absorbance changes as shown by the downward  
178 negative peaks in the indicated region in figure 1. This is very common in materials that  
179 contain high silicate content or similar and/or contain highly scattering components such as  
180 flyash or graphene oxide.. . From the FTIR spectrum of the rGO-geopolymeric matrix, it  
181 can be seen that the GO has undergone chemical reduction of the hydroxyl and carbonyl  
182 functional groups, whereas the unreactive C-H peaks at  $1500\text{ cm}^{-1}$  remained largely  
183 unchanged due to their inert nature.

184 Figure 2 shows the FTIR spectra between  $2000\text{-}650\text{ cm}^{-1}$  of both the plain and the rGO  
185 reinforced geopolymers. As shown in this figure, the presence of the rGO in the  
186 geopolymeric matrix increased the moderately absorbing band at  $\sim 1425\text{ cm}^{-1}$ , this can be  
187 assigned to a C-H vibration. In addition, the Si-O bonds increased the absorbance at  $1000\text{-}$   
188  $1200\text{ cm}^{-1}$  as a direct result of the chemical reaction of the sodium silicate with the matrix  
189 components creating new Si-O<sub>2</sub> based cross-linking with fly ash or rGO. The change in  
190 absorbance is marked large considering the rGO addition was a mere 0.35wt%

191 Figure 3 further confirms that the pristine GO sheets have been reduced during the  
192 processing of the geopolymers. This figure compares the FTIR spectra of the isolated  
193 unreduced/pristine GO sheets with the difference spectra of the geopolymer with and without  
194 the incorporation of 0.35wt% GO. The dotted blue line is the difference between each single  
195 point of the spectra presented in Fig. 3 for the full spectral region. As can be seen from this  
196 figure, there is a clear attenuation of hydroxyl and carbonyl functionalities between  $3000$  and  
197  $3750\text{ cm}^{-1}$  and, between  $1650$  and  $1800\text{ cm}^{-1}$ , respectively. High attenuation of the hydroxyl  
198 and carbonyl groups indicating reduction of GO by the alkali NaOH [22, 23] as shown in the  
199 difference spectra. The non-reducible functional groups of the GO are still present in the  
200 difference spectra at  $3000\text{-}2850\text{ cm}^{-1}$  and at  $1200\text{-}1500\text{ cm}^{-1}$ , these are the unreactive C-H  
201 type bonds. Previous studies have shown that during processing with NaOH or strong alkali,



202 the GO sheets undergo deoxygenation and the number of carbonyl and hydroxyl groups are  
203 then reduced. This leads to the formation of highly reduced GO sheets (rGO) with mechanical  
204 and electrical properties superior to those of pristine GO sheets [22, 23]. The authors suggest  
205 that the GO incorporated into the geopolymer actually contains the in-situ reduced-GO cross-  
206 linked graphene based material within the geopolymer matrix thereby increasing mechanical  
207 and electrical properties. Additionally greatly lowering porosity.

208 The mechanical properties of the rGO-geopolymeric composites are highly dependent on  
209 the physical and chemical interactions between the rGO and the matrix. These interactions  
210 include both mechanical and chemical covalent bonding. The mechanical interaction is due to  
211 the mechanical interlocking between the textured (wrinkled) morphology of the rGO sheets  
212 and the matrix. The Si-O covalent bond absorbance augmentation is likely to be the cross-  
213 linking bridging between the fly ash and the rGO sheets. The authors suggest that the *in-situ*  
214 cross-linked particles in the form of  $[-Si-O-]_x[rGO]_y[-O-Si-]_z$  (with  $x \geq 1$ ,  $y \geq$  and  $z \geq 0$ ) is  
215 formed in the rGO-geopolymeric matrices. The silicon has the ability to further bond to the  
216 fly ash or rGO, this creates a diverse particle size, shape and morphologies enabling virtually  
217 any pore or void to be filled. Moreover unreacted hydroxyl groups on the GO or fly ash can  
218 undergo further cross-linking to become larger crack filling and bridging particles.

### 219 3.2. Morphology

220 The morphology of the fly ash is well known and is a wide distribution of mostly spherical  
221 particles that encompasses the submicron to the micron range. These particles are the  
222 dominant base for both types of geopolymers and are highly siliceous. Figure 4a shows the  
223 SEM micrograph of the rGO sheets, clearly there is a highly textured morphology enabling  
224 the rGO to morph around complex shapes and interact mechanically. The chemical alkaline  
225 reduction of GO to rGO (reduced form) removes the oxygen rich functional groups as well as  
226 causing the high degree of wrinkling and folding [24]. Wrinkles have a positive effect on the

227 mechanical properties of rGO reinforced geopolymers, as they tend to improve the  
228 interlocking mechanism within the matrix [25]. Figures 4b, 4c and 4d show the morphology  
229 of the geopolymeric suspensions containing 0.35-wt% rGO. In Fig. 4b, the sub-micron fly  
230 ash spheres are randomly deposited on the rGO sheets. The rGO sheets exhibited random  
231 holes and tearing. From Fig. 4b, it can be seen that the size the submicron fly ash spheres  
232 matches the size of the holes, suggesting that some of the particles pierced the rGO sheets  
233 during processing, resulting in random holes. Fig. 4c shows the fly ash particles covered  
234 with thin rGO sheets, forming hybrid clusters. This can be attributed to the effect of cross-  
235 linking and functionalization on the surface area of the rGO sheets and the fly ash particles  
236 [26, 27]. The exchange between the two materials typically occurs through electric induction  
237 (also known as polarization) causing the rGO sheets to adsorb onto the fly ash particles. The  
238 strain induced by the largest fly ash particles also caused the folding of the flexible rGO  
239 sheets around the largest fly ash particles, producing shapes like a “mushroom” as shown in  
240 Figs. 4c and 4d. One possible interpretation for this observation is that the rGO sheets  
241 inherently contain both crystalline and amorphous regions. The amorphous region is less  
242 stable, more soluble and relatively disordered thus becomes more amenable to deform when  
243 the fly ash particles push against it.

244 Figures 4c and 4d also show that the pores and voids were substantially filled and bridged  
245 at 0.35-wt%, partially due to the formation of the cross-linked particles. The pore filling with  
246 the malleable rGO sheets also reduced the porosity and presence of voids. Additionally, the  
247 small scraps of rGO sheets that were moved by the fly ash particles also filled and bridged the  
248 voids and hollow spaces in the matrix as depicted in Fig. 5.

### 249 *3.3. Mechanical characterization*

250 Figure 6 shows the load-deflection responses of the geopolymeric beams. The beams were  
251 initially preloaded up to a deflection of 0.2 mm to ensure good contact with the load and

252 support points. The load-deflections results indicated the significant increase in stiffness and  
253 load-carrying capacity of the beams due to the addition of rGO sheets. This is attributed to  
254 the stiffness and surface area of the rGO sheets. The wrinkled texture of the rGO sheets also  
255 played a positive role in the load transfer between the rGO sheets and the geopolymeric  
256 matrix, as it tends to enhance the mechanical interlocking coupled with chemical cross-  
257 linking type bonding.

258 The deflection at failure decreased as the rGO sheet content increased. This can be  
259 explained as follows (see Fig. 7): at low rGO sheet contents, the sheets are generally  
260 separated and randomly dispersed within the matrix with a slight negative effect on the  
261 mechanical deformation. At medium rGO contents, the sheets are joined together with some  
262 overlapping each other, producing stiff plates rigidly bonded to the matrix. In this case, the  
263 matrix is restrained from movement and as a result the deflection is reduced. Severe  
264 restacking of sheets occurs at high rGO sheet contents due to van-der-Waals forces (van-der-  
265 Waals forces from NaOH-induced attenuation of hydroxyl groups) where the sheets are  
266 stacked on top of each other to form rigid laminates. This further restricts the movement of  
267 the matrix, causing the beams to fail in a brittle manner. This behavior has also been found in  
268 other graphene-based polymer composites [28, 29].

269 The average mechanical properties are given in Fig. 8. A noticeable flexural strength gain  
270 of 49%, 130% and 134% was achieved for beams with rGO sheet concentrations of 0.10, 0.35  
271 and 0.50-wt%, respectively. A significant increase in stiffness was also obtained. The  
272 increase was about 107%, 365% and 376% for rGO contents of 0.10, 0.35 and 0.50-wt%,  
273 respectively. The flexural toughness was improved by 12%, 56% and 48% for rGO contents  
274 of 0.10, 0.35 and 50-wt%, respectively. The geopolymers with 0.35 and 0.5-wt% rGO  
275 exhibited somewhat similar mechanical properties, indicating a mechanical percolation  
276 threshold was achieved at 0.35-wt%. These results are in line with previous studies on

277 graphene composites [30, 31]. These studies have shown that graphene sheets can enhance  
 278 the mechanical properties of composites at significantly lower graphene concentrations in  
 279 comparison to CNTs. For example, 0.125-wt% of graphene increased the tensile strength and  
 280 the Young's modulus of polymers by 45% and 50%, respectively, whereas, 1-wt% of CNTs  
 281 increased the tensile strength and the Young's modulus of polymers by 15% and 30%,  
 282 respectively [30].

### 283 3.4. Toughening and load transfer mechanisms

284 The rGO morphology and the shear lag model can be used to quantify the load transfer  
 285 mechanism in the rGO-geopolymeric composites. The relationship between the strain  $\varepsilon_p$  in  
 286 the rGO sheet and the geopolymeric matrix strain  $\varepsilon_m$ , can be written as [32]:

$$287 \quad \varepsilon_p = \varepsilon_m \left[ 1 - \frac{\cosh\left(ns \frac{x}{l}\right)}{\cosh(ns/l)} \right] \quad (4)$$

$$288 \quad n = \sqrt{\frac{2G_m t}{E_p T}}$$

289 where  $G_m$  is the shear modulus of the matrix,  $E_p$  is the Young's modulus of the rGO sheet,  $l$  is  
 290 the length of the rGO sheet in the  $x$  direction,  $t$  is the thickness of the rGO sheet,  $T$  is the total  
 291 thickness of the matrix and  $s$  is the aspect ratio of the rGO sheet ( $l/t$ ) in the  $x$  direction. In  
 292 Eq. (4), the parameter  $n$  is an effective measure of the interfacial stress transfer efficiency and  
 293 the product  $ns$  depending on both the morphology of the rGO sheet and the degree of  
 294 interaction with the hosting geopolymeric matrix [32].

295 The morphology of the wrinkled rGO sheet shown in Fig. 6a can be characterized by the  
 296 wavelength  $\lambda$  and the amplitude  $A$  of the wrinkles as [33]:

$$297 \quad \lambda^4 = \frac{4\pi^2 \nu (tl)^2}{3(1-\nu^2)\varepsilon} \quad (5)$$

298 
$$A^2 = \left[ \frac{16\varepsilon\nu}{3\pi^2(1-\nu^2)} \right]^{1/2} tl \quad (6)$$

299 where  $\nu$  is the Poisson's ratio of the rGO sheet and  $\varepsilon$  is the compressive strain in the rGO  
 300 sheet from the exfoliation process.

301 The shear stress between the rGO sheet and the geopolymeric matrix is given by [32]:

302 
$$\tau = nE_p \varepsilon_m \frac{\sinh\left( ns \frac{x}{l} \right)}{\cosh(ns/2)} \quad (7)$$

303 As can be seen from Eqs. (4), (5), (6) and (7), the high aspect ratio  $s = l/t$ , the Young's  
 304 modulus  $E_p$  and the morphology of the rGO sheet are the main key factors that significantly  
 305 contributed to the improved mechanical properties of rGO reinforced geopolymers  
 306 composites .

307 The toughening mechanism in graphene composites is not well understood and research on  
 308 this topic is limited. This can be attributed to the difficulty of identifying crack pinning or  
 309 crack bridging by the graphene sheets using traditional analysis tools such as SEM [34].  
 310 Rafiee et al. [31] have shown that the toughening mechanism in composites reinforced with  
 311 graphene is different from that reinforced with CNTs. In CNTs, the toughness is dominated  
 312 by the crack-bridging mechanism where the energy is dissipated by the frictional pullout of  
 313 the bridging CNTs from the matrix. However, in graphene, the toughening mechanism is  
 314 crack deflection. In this case, microcracks are deflected and twisted when they run into a  
 315 rigid graphene sheet. Rafiee et al. [31] reported that this mechanism increases the total  
 316 fracture surface leading to greater energy absorption. Although further validation studies are  
 317 needed to identify the toughening mechanism, the experimental results presented herein  
 318 suggest that crack deflection may have occurred in the rGO-geopolymeric composites and it  
 319 is reflected in their high Young's modulus and flexural toughness (see Fig. 8).

320 **4. Conclusions**

321 New rGO-geopolymeric composites with enhanced properties were successfully produced  
322 using the same mixing method used to make OPC. The interaction of the GO sheets with the  
323 alkaline solution used to process the geopolymeric composites yielded highly reduced and  
324 cross-linked GO sheets. The addition of these rGO sheets into geopolymers at very low  
325 contents simultaneously improved the mechanical properties and reduced the overall porosity  
326 of geopolymers. The malleable rGO sheets and the small scraps of rGO sheets that were  
327 moved by the fly ash particles filled the voids and hollow spaces in the matrix. The  
328 incorporation of rGO sheets improved the mechanical properties of the geopolymeric  
329 composites as a result of their 2-dimensional structure and good chemical bonding with the  
330 matrix. The rGO concentration of 0.35-wt% yielded the highest mechanical properties. At  
331 this concentration, the flexural strength and Young's modulus increased by 134% and 376%,  
332 respectively. A moderate increase in toughness (as much as 56%) was obtained due to the  
333 restacking of the rGO sheets and the formation of stiff hybrid of rGO-fly ash fillers within the  
334 matrix. The rGO-geopolymeric composites can be an environmental friendly and economical  
335 alternative to OPC due to their low green-house gas emissions and improved mechanical  
336 properties. The *in-situ* reduction of GO makes geopolymers ideal candidates for high  
337 performance and (potentially) self-sensing structural materials for various applications such as  
338 bridges, roadways and smart structures with inherent increased durability due their near pore-  
339 free morphology.

#### 340 **References**

- 341 [1] Sakulich AR. Reinforced geopolymer composites for enhanced material greenness and  
342 durability. *Sustainable Cities and Society* 2011; 1:195-210.
- 343 [2] Hardjito D. Studies on fly ash-based geopolymer concrete. PhD thesis 2005, Curtin  
344 University of Technology, Australia.

- 345 [3] Bakharev T. Resistance of geopolymer materials to acid attack. *Cement and Concrete*  
346 *Research* 2005; 35(5): 658-670.
- 347 [4] Bakharev T. Durability of geopolymer materials in sodium and magnesium sulfate  
348 solutions. *Cement and Concrete Research* 2005; 35(6): 1233-1246.
- 349 [5] Shankar HS and Khadiranaikar RB. Performance of geopolymer concrete under severe  
350 environmental conditions. *International Journal of Civil and Structural Engineering* 2012;  
351 3(2): 396-407.
- 352 [6] Pan Z, Sanjayan JG and Collins F. Effect of transient creep on compressive strength of  
353 geopolymer concrete for elevated temperature exposure. *Cement and Concrete Research*  
354 2014; 56: 182-189.
- 355 [7] Duxson P, Lukey GC and van Deventer JSJ, Thermal evolution of metakaolin  
356 geopolymers: part 1—physical evolution. *Journal of Non-Crystalline Solids* 2006; 352(52-  
357 [8] Uddin F, Shaik A. Review of mechanical properties of short fibers reinforced geopolymer  
358 composites. *Construction and Building Materials* 2013; 43: 37-49.
- 359 [9] D.P. Dias DP, Thaumaturgo C. Fracture toughness of geopolymeric concretes reinforced  
360 with basalt fibres. *Cement and Concrete Composites* 2005, 27: 49–54
- 361 [10] Mackenzie KJD, Bolton MJ. “Electrical and mechanical properties of aluminosilicate  
362 inorganic polymer composites with carbon nanotubes. *Journal of Material Sciences*  
363 2009; 44(11): 2851-2857.
- 364 [11] Saafi M, Andrew K, Tang PK, McGhon D, Taylor S, Rahman M, Yang S, Zhou X.  
365 Multifunctional properties of carbon nanotube/fly geopolymeric nanocomposites.  
366 *Construction and Building Materials* 2013; 49: 46-55.
- 367 [12] Xia Z, Riester L, W.A Curtin WA, Lia H, Sheldon BW, Liang J, Chang B, Xu JM.  
368 Direct observation of toughening mechanisms in carbon nanotube ceramic matrix  
369 composites. *Acta Materialia* 2004; 52 (4): 931-944.

- 370 [13] Collins F, Lambert J, Duan WH. The influence of admixtures on the dispersion,  
371 workability, and strength of carbon nanotube-OPC paste mixtures. *Cement and Concrete*  
372 *Composites* 2012; 34(2): 201–207.
- 373 [14] Abu-Al-Rub RK, Tyson BM, Yazdanbakhsh A, Grasley, Z. Mechanical properties of  
374 nanocomposite cement incorporating surface-treated and untreated carbon nanotubes and  
375 carbon nanofibers. *ASCE Journal of Nanomechanics and Micromechanics* 2012; 2(1): 1-  
376 6.
- 377 [15] Porwal, H., Grasso S, Reece M. Review of graphene–ceramic matrix composites.  
378 *Advances in Applied Ceramics* 2013; doi 10.1179/1743676113Y.0000000095.
- 379 [16] Yang Y, William R, Xinyu, Huang X, Li X. Enhancing graphene reinforcing potential in  
380 composites by hydrogen passivation induced dispersion. *Scientific Reports* 2013; 3:  
381 2086; doi: 10.1038/srep02086.
- 382 [17] Zhu Y, Murali S, Cai W, Li X, Won SJ, Potts, JR, Ruoff RS. Graphene and graphene  
383 Oxide: synthesis, properties and applications. *Advanced Materials* 2010; 22(35), 3906–  
384 3924.
- 385 [18] Stankovich S, Piner RD, Nguyen ST, Ruoff RS. Synthesis and exfoliation of isocyanate-  
386 treated graphene oxide nanoplatelets. *Carbon* 2006; 44(15) 3342-3347.
- 387 [19] Kim DH, Yun YS, Jin HJ. Difference of dispersion behavior between graphene oxide  
388 and oxidized carbon nanotubes in polar organic solvents. *Current Applied Physics* 2012;  
389 12(3): 637-642.
- 390 [20] Kim H, Abdala AA, Macosko, CW. Graphene/polymer nanocomposites.  
391 *Macromolecules* 2010; 43(16): 6515-6530.
- 392 [21] Du J, Cheng HM. The Fabrication, properties and uses of graphene/polymer composites  
393 *Macromol Chem Phy* 2012; 213: 1060-1077.



- 394 [22] Thomas H R, Valles C, Young RJ, Kinloch IA, Wilson NR, Rourke PJ. Identifying the  
395 fluorescence of graphene oxide. *Journal of Mater Chem C* 2013, 1: 338-342.
- 396 [23] Fan X, Peng W, Li Y, Wang S, Zhang G, Zhang F. Deoxygenation of exfoliated graphite  
397 oxide under alkaline conditions: a green route to graphene preparation. *Adv Mater* 2008;  
398 20: 4490-4493.
- 399 [24] Bai S, Shen X, Zhu G, Yuan A, Zhang J, Ji Z, Qiu D. The influence of wrinkling in  
400 reduced graphene oxide on their adsorption and catalytic properties. *Carbon* 2013; 60:  
401 157-168.
- 402 [25] Galpaya D, Wang M, Yan C, Liu M, Motta N, Waclawik ER. (2013) Fabrication and  
403 mechanical and thermal behaviour of graphene oxide/epoxy nanocomposites. *Journal of*  
404 *Multifunctional Composites* 2013, 1(2): 91-98.
- 405 [26] ] Hsu TC. Adsorption of an acid dye onto fly ash. *Fuel* 2008; 87:3040-3045.
- 406 [27] Willner MR. Metal removable by sodium graphene oxide. Master of Science in  
407 Environmental Engineering 2012, University of Notre Dame, Indiana.
- 408 [28] Li Z, Young RJ, Kinloch IA. Interfacial stress transfer in graphene oxide  
409 nanocomposites. *ACS Appl Mater Interfaces* 2013; 5: 456-463..
- 410 [29] Zhao X, Zhang Q, Chen D. Enhanced mechanical properties of graphene-based  
411 poly(vinyl alcohol) composites. *Macromolecules* 2010; 43: 2357–2363.
- 412 [30] Rafiee MA, Rafiee J, Srivastava I, Wang Z, Song H, Yu, ZZ, Koratkar N. Fracture and  
413 fatigue in graphene nanocomposites. *Small* 2010; 6(2), 179–183.
- 414 [31] Rafiee MA, Rafiee J, Srivastava I, Wang Z, Song H, Yu ZZ, Koratkar N. Enhanced  
415 mechanical properties of nanocomposites at low graphene content. *ACS Nano* 2009;  
416 3(12): 3884-3890.

- 417 [32] Gong L, Kinloch IA, Young RJ, Riaz I, Jalil R, Novoselov KS. Interfacial stress  
418 transfer in a graphene monolayer nanocomposite. *Advanced Materials* 2010; 22(24):  
419 2694–2697.
- 420 [33] Tapasztó L, Dumitrica T, Jin-Kim S, Nemes-Incze P, Hwang C, Biró LP. Break-down of  
421 continuum mechanics for nanometer-wavelength rippling of graphene. *Nature Physics*  
422 2012; 8: 739-741.
- 423 [34] *Graphene in composite materials: synthesis, characterization and applications*. Edited by  
424 Koratkar N, March 2003, DEStech Publications, Inc.
- 425
- 426

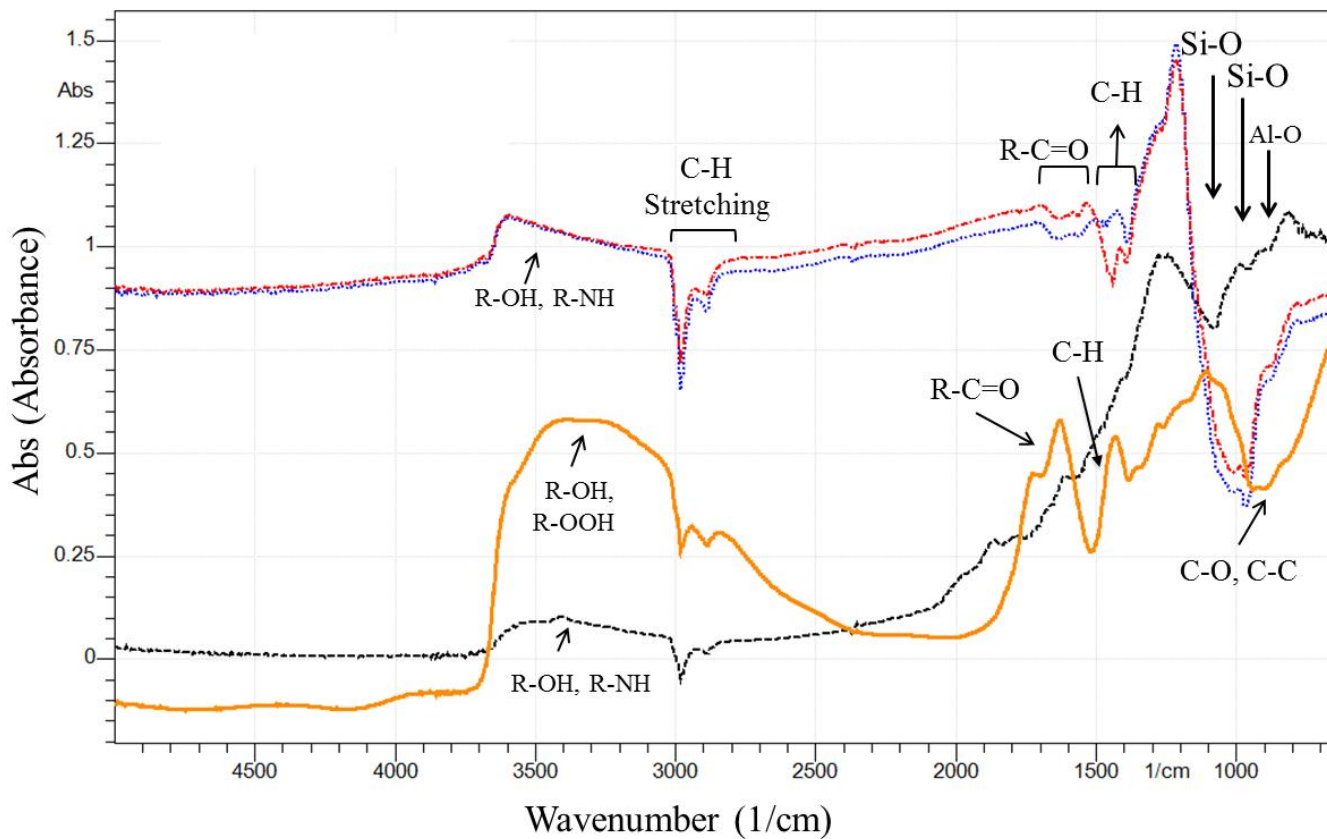


Fig. 1 – Diffuse FTIR spectra of fly ash (black line), un-reduced GO sheets (orange line), plain geopolymeric composites (red line) and rGO incorporated into the geopolymeric composites (blue line).

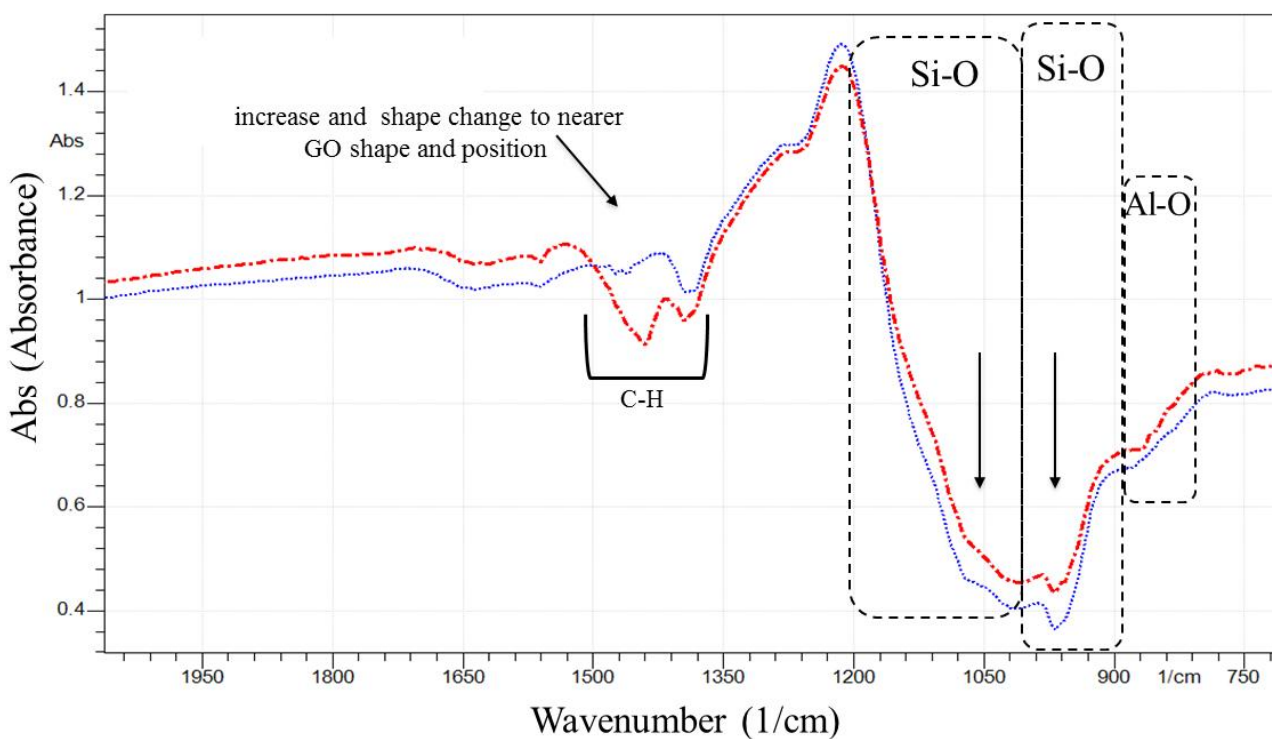


Fig.2- Diffuse FTIR spectra between 2000 and 650 1/cm of plain geopolymeric composites (red line) and rGO incorporated into the geopolymeric composites (blue line).

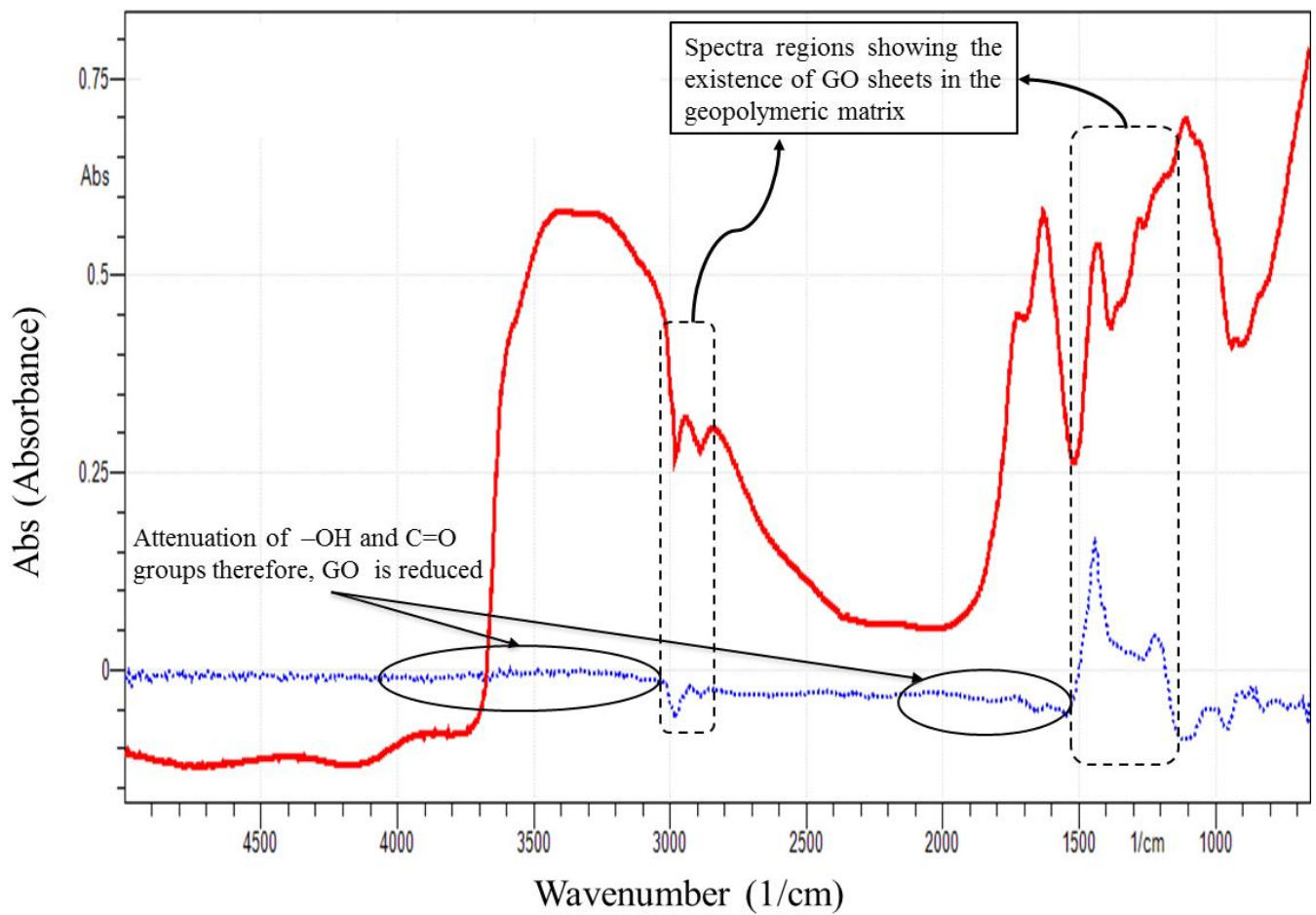


Fig. 3- Diffuse FTIR spectra of un-reduced GO (red line) in comparison to the difference spectra (blue line) of the geopolymer with and without rGO.

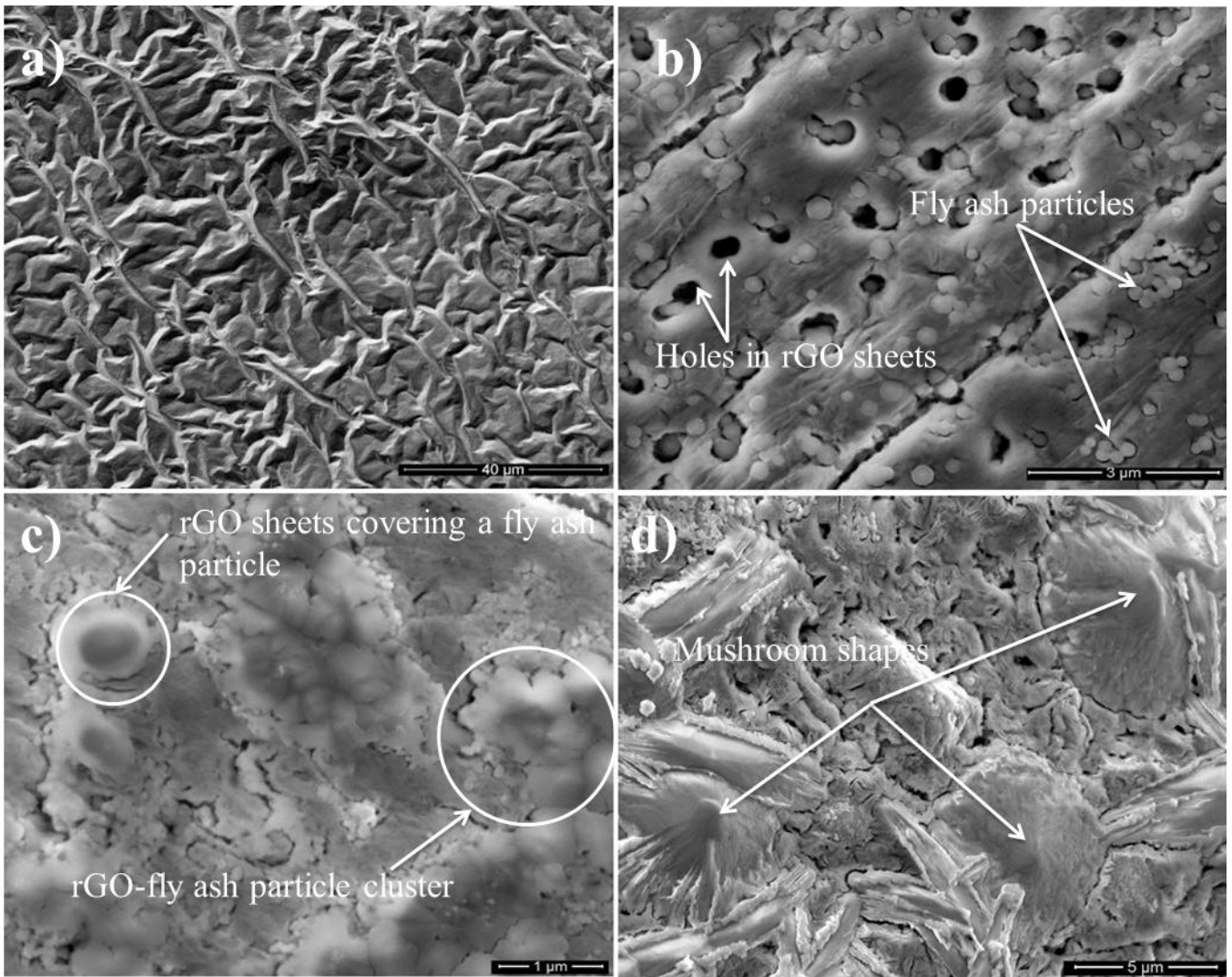


Fig.4 - SEM micrographs (a) morphology of rGO sheets (b) 0.35-wt% GO sheets interaction with submicron fly ash, (c) 0.35-wt% GO sheets covering submicron fly ash particles, (d) 0.35-wt% GO sheets interaction with larger fly ash particles.

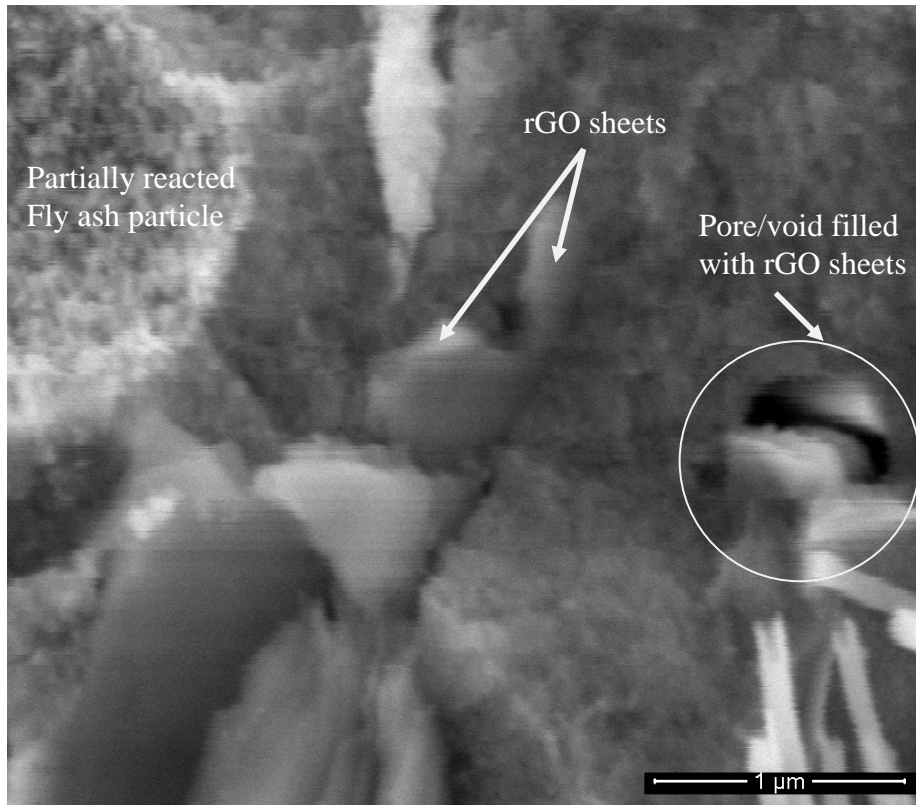


Fig. 5- SEM micrograph showing 0.5-wt% rGO sheets filling pores and voids.

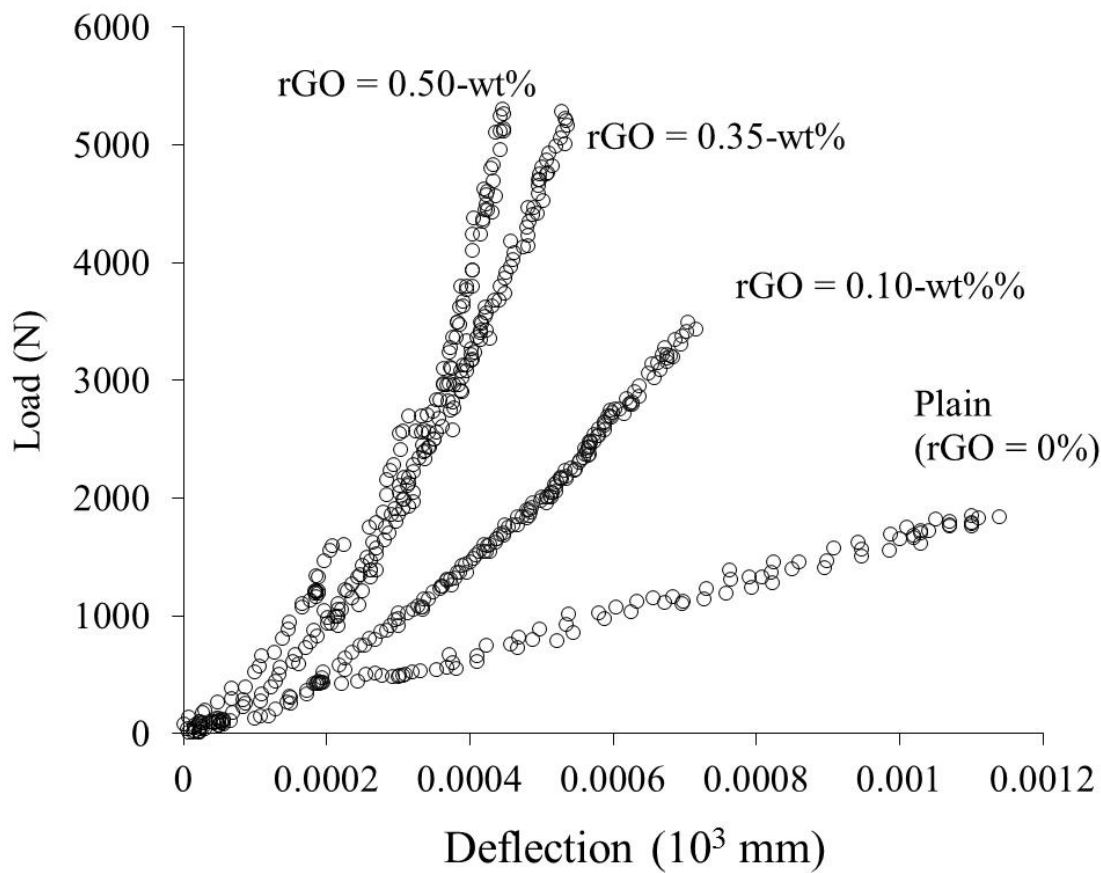


Fig.6-Load-deflection response of the rGO-geopolymeric composite beams.

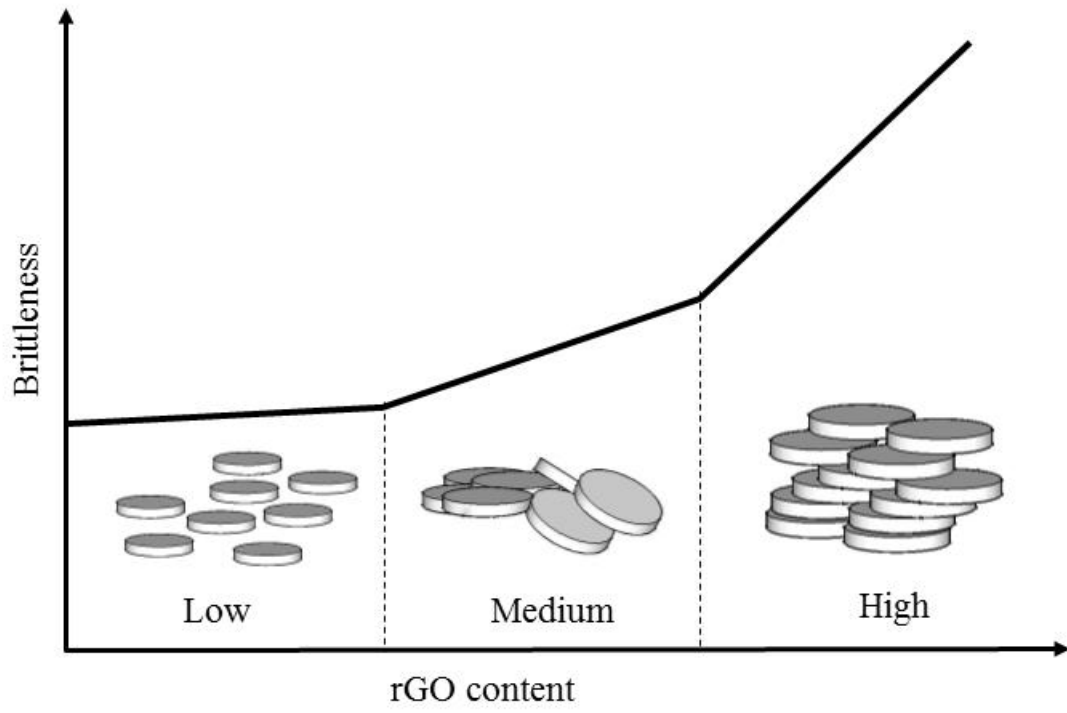


Fig. 7-Effect of rGO content on the brittleness of rGO-geopolymeric composites

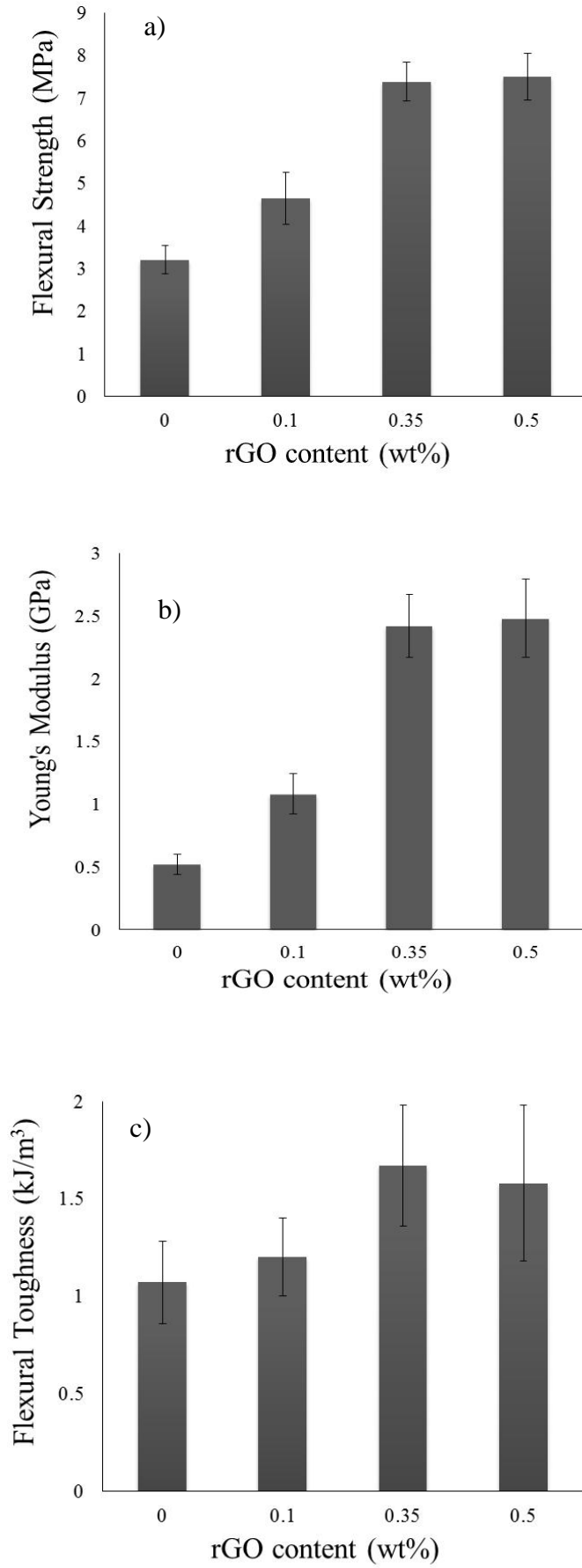


Fig.8- Mechanical properties of rGO-geopolymeric composites. a) flexural strength, b) Young's modulus, c) flexural toughness.



**Table 1.** Main chemical composition of fly ash (wt%)  
(as provided by the supplier)

Element	Weight %
Silicon dioxide, SiO <sub>2</sub>	53.50
Aluminium oxide, Al <sub>2</sub> O <sub>3</sub>	34.30
Iron oxide, Fe <sub>2</sub> O <sub>3</sub>	3.60
Calcium oxide, CaO	4.40
Loss of Ignition	2.00